CHAPTER-5

Crystalline/crystalline interfaces in

$Li(Ni,Mn)_xO_y$ / Nb-$SrTiO_3$ thin films

5.1 Introduction

Continuously diminishing fossil fuel resources and stringent regulation towards environmental protection have led to the search for alternative energy resources. [274–280]. The search for robust and sustainable technologies through the invention of energy storage devices was initiated by Alessandro Volta way back in early nineteenth century, which led to the commercialization of lithium metal batteries in the later part of the twentieth century [281,282]. However, the stability and safety are still a challenge, even though its efficacy was understood. Safety refers to the explosion of the batteries due to excessive heating and the toxic nature of the materials (Co/Ni) used in them. Stability pertains to the dissolution of the electrode and the phase transformation that occurs during charging and discharging [220,283,284]. Continued efforts in this direction gave birth to the lithium ion batteries (LIBs). Challenges to meet the demand of efficiency, energy density, safety etc., have been the driving force for research [279,285–287].

Rechargeable LIBs have emerged as a potential candidate to solve the existing problems [288–290]. The major research activity on LIBs till now is focused on increasing its overall performance in terms of various parameters such as operating voltage, current density, energy density, rate performance, capacity, surface to volume ratio, lifetime etc.[195,287,289]. The LIBs should also be safe and environmentally compatible as well. There are several design options for LIB cathodes and alteration of properties is much readily available by adopting a new cathode design strategy [195]. So, researchers have oriented their work mostly in developing and exploring the cathode material for LIBs. These cathode materials based LIBs have found their way in various applications such as portable electronic devices, drug delivery, MEMS, hybrid (HEVs) and fully electric

vehicles (EVs) etc. [291,292]. This necessarily means that there is no universally acceptable design option, however, it has to be application specific.

The performance of LIBs inherently depends on the characteristics of the cathode materials and its functionality can be tuned by deciphering the underlying transport mechanism in the cathode under operating conditions. Li based transition metal oxides like $LiMn_2O_4$ with spinel structure (Space group: $Fd\bar{3}m$) and $LiMO_2$ (*M*= Ni, Co etc.) (Space group: $R\bar{3}m$) with layered structures have been identified as candidate materials [293]. Even though the electro-chemical behavior of $LiMn_2O_4$ is quite similar to $LiCoO_2$ coupled with eco-friendliness, abundance, low-cost and low toxicity [MSDS#7440-48-4, Aldrich; MSDS#7440-02-0, Aldrich]. $LiCoO_2$ is the preferred cathode material due to its less capacity fading over cycling. Its operating voltage is also higher. $LiNiO_2$ is preferred over $LiCoO_2$ pertaining to its excellent capacity, higher energy density and lower cost and high reversible capacity. Efficient Li-ion extraction takes place in $LiNiO_2$ at lower operating voltage compared to $LiCoO_2$ [292,294]. Over the last few years, it has been realized that the layered composite cathode materials have excellent realistic capacity of 200-250 $mAhg^{-1}$, which is ~ 65-75 $mAhg^{-1}$ more than the other traditional LIBs cathode materials [295,296]. So far high temperature applications are concerned, the structural stability of $LiNiO_2$ and $LiMn_2O_4$ cannot be assured. Owing to the oxygen evolution at higher temperature, the tendency of $LiNiO_2$ towards delithiated states is higher and $LiMn_2O_4$ tends to transform into the Li-rich (Li_2MnO_3) phase. Moreover, due to these structural transformations, $LiNiO_2$ shows huge capacity loss just after the first charge/discharge. $LiMn_2O_4$, in contrast Mn^{3+} ions displays decomposition in a disproportionate manner from Mn^{3+} to Mn^{4+} state [297]. In addition to this, presence of Mn^{2+} is also reported [284]. The two taken together is expressed as: $Mn^{3+} \rightarrow Mn^{4+}$ and Mn^{2+}. Such structural instability at

elevated temperature is understood to be a major impediment in the successful commercial exploitation of this cathode material. Additionally, the surrounding environment may also affect the battery performance by degrading the cathode materials [194]. The presence of trace amount of moisture sets up a cyclic reaction between the cathode material and the electrolyte $LiPF_6$, which leads to metal dissolution and fluoride formation. Partial substitution of transition metal from the host cathode by Co and/or Mn and Al, coating the cathode surface by oxides e.g. Al_2O_3, ZrO_2, MgO, SiO_2, ZnO, TiO_2, $AlPO_4$ etc., are the potential solutions, which retard the metal dissolution and keep the charge transfer characteristics intact [286,290,292].

Controlled synthesis of the cathode material improves its morphology and crystallinity [298]. Favorable morphology of the cathode material results in the bell shaped curve of the deposited SEI (solid electrolyte interface) layer and unfavorable morphology leads to the dendritic shape of SEI layer [299]. Additionally, significant volume of work in the literature has confirmed that the {111} faces are less prone to metal dissolution compared to {100} and {110} faces in case of oriented growth of the cathode material [300]. Moreover, the area ratio of different facet planes may change with the shape of the cathode materials particle e.g. spherical, octahedron, truncated octahedron etc., and it significantly alters the performance of the battery. As a consequence, the research on epitaxially grown interfaces of electrode-electrolyte, electrolyte-collector is rapidly gaining importance [103,301]. The localized structural changes from bulk to the surface within the cathode material due to the migration of transition metals such as Ni, Mn, Co etc. , have not been understood properly [171,302]. The possible vacancy paths encountered by the transition metals while migrating through intra and inter Li-layer is not clearly understood. In order to alleviate the above mentioned problems, an entirely different solution involves the modification in the

materials architecture of the cathode i.e. design compositionally graded or core-shell cathodes [279,296,297]. Although, enhanced performance, excellent thermal stability and better cyclability have been achieved in core-shell and compositionally graded cathodes; compositional change induced local phase transformation, cation mixing, localized volume changes during lithiation and delithiation, and evolution of interface structure is not quite understood. Moreover, such particulate agglomerates have been mostly synthesized by solution chemistry technique. There have been a few attempts to synthesize such cathodes in the form of a thin film onto a suitable collector and understand their phase evolution, state of ordering, interface structure and correlating such microstructural features to the origin of electro-chemical activity of the cathode.

In the present work, $Li(Ni, Mn)_xO_y$ compositionally graded cathode films have been synthesized by pulsed laser deposition (PLD) technique on to (111)-cut single-crystal 0.5 wt% Nb-doped $SrTiO_3$ (Nb:STO) substrates. PLD technique has been chosen in order to achieve the target composition. The PLD deposited film is expected to have high quality and better epitaxy with bigger grain size [220,303,304]. Phase evolution, state of ordering, interface structure, orientation relationship have been studied at the atomic scale by atomic resolution analytical transmission electron microscopy (TEM). Finally, the effect of the microstructural features and its potential correlation with the origin of electro-chemical properties has been discussed.

5.2 Experiments

5.2.1 Thin film deposition

The details of the starting materials and deposition process is already provided in chapter 2 of this thesis. $LiNiO_2$ is stoichiometric in composition. Prior to deposition, the substrate surface was ultrasonically cleaned in methanol and isopropanol, and was loaded in the

deposition chamber. Initially $LiNiO_2$ was deposited on the substrate for 180s and subsequently the deposition time for $LiNiO_2$ was reduced in steps of 10% and that time was used for deposition from the $LiMnO_x$ target. A schematic representation of deposition schedule from different targets in terms of time is given in figure 5.1.

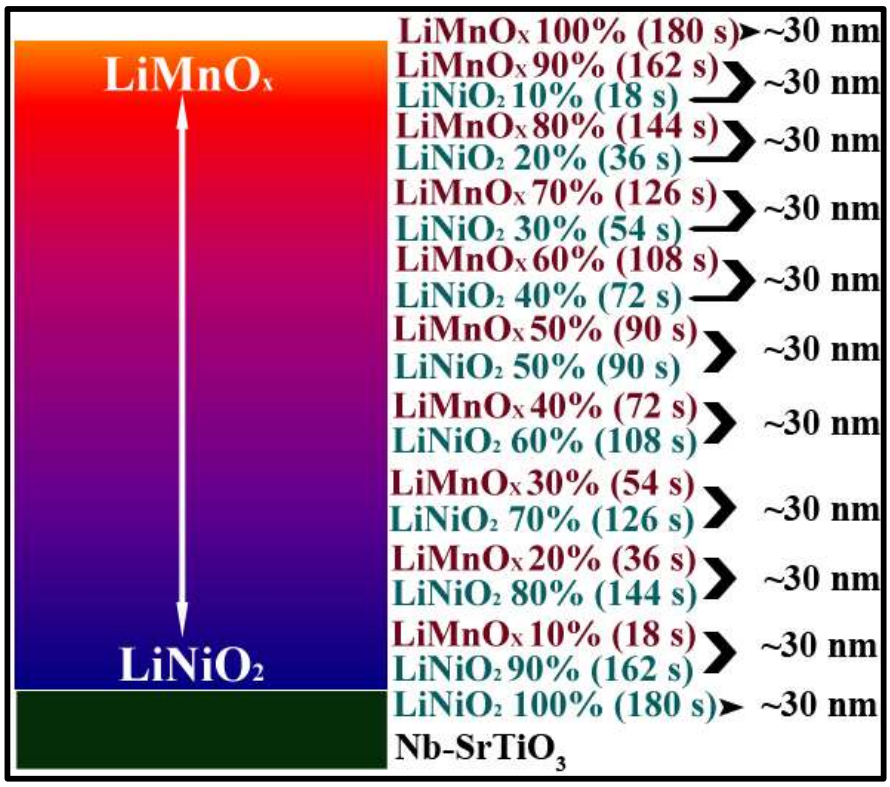

Figure 5.1: *Schematic representation of the deposition schedule of $LiNiO_2$ and $LiMnO_x$ on 111 single-crystal Nb-doped $SrTiO_3$ (Nb:STO) substrate by combinatorial pulse laser deposition.*

This particular deposition schedule was maintained in order to deposit a film which was Ni-rich towards the substrate and it gradually becomes Mn-rich towards the surface of the film. This deposition schedule should lead to a compositionally graded thin film which is Ni-rich near the substrate that gradually depletes and in turn it becomes Mn-rich towards the surface of the film producing ideally a sigmoidal composition profile for Ni and Mn provided the deposition rate remains equal from both the targets. Otherwise, the film should

be predominantly Ni-rich towards the substrate and Mn-rich towards the surface of the film. The targets were placed at a distance of 68 mm from the substrate. The film was deposited in 50 mTorr oxygen atmosphere at 620 ºC substrate temperature with a 10 Hz laser (source: Nd:YAG) of energy density 0.8 J/cm^2. Laser energy was 620 mJ, laser spot size was 0.125 cm^2.

5.2.2 Experimental electron microscopy

Electron transparent conventional cross-section samples were prepared by grinding, dimpling followed by ion beam thinning of the cross-section. Ion beam polishing was carried out with a Gatan PIPS with Ar-ions operated under 5keV. While milling, the sample was cryogenically cooled to liquid nitrogen temperature, it was milled at low angle of inclination. The sample was milled for five minutes and it was looked under the stereo microscope in order to prevent the generation of perforation and creation of damage layer. Diffraction contrast imaging and diffraction experiments were carried out in a JEOL 3010 TEM operating at 300 kV. High resolution phase contrast imaging, electron energy loss spectroscopy, STEM-EDS mapping and line scan of the thin film cross section was carried out in a FEI Titan with super twin lens (C_s=1.2 mm) at 300 kV. Negative aberration corrected phase contrast imaging was also carried out. Various correction parameters during imaging were as follows: C_s= (-0.00683) mm, A1=0.7246 nm, A2=46.68 nm, B2=13.8 nm, A3=295.3 nm, S3=90.35 nm. The terms have usual meaning.

5.2.3 Multislice simulation and electron diffraction

High-resolution images and diffraction patterns were simulated for cubic $LiMn_2O_4$ spinel and rhombohedrally distorted $LiNiO_2$ layered structure by JEMS. The images along particular zone axis were simulated by multislice method keeping various parameters in commensurate with those of experiments. Diffraction pattern was computed under multiple

beam dynamical condition and the crystal thickness was considered to be 20 nm. Crystallographic details of the phases which has been used for simulation are given in Table 5.1.

Table 5.1: *Structural parameters used in multislice simulation.*

S. No.	Structure	Lattice Parameter (nm)	Space Group (No.)	Wyckoff Positions (site)	Coordinates	Occ. (%)	Ref.
1.	$LiMn_2O_4$	a= 0.824	$Fd\bar{3}m$	8a (Li) 16d (Mn) 32e (O)	(0,0,0) (0.625,0.625,0.625) (0.361,0.361,0.361)	1 1 1	01-083-5056
2.	$LiNiO_2$	a= 0.288 c=1.419	$R\bar{3}m$	3a (Ni) 3b (Li) 3c (O) 3c (O)	(0,0,0) (0,0,0.5) (0,0,0.25) (0,0,0.75)	1 1 1 1	01-083-9893
3.	$SrTiO_3$	a= 0.390	$Pm\bar{3}m$	1a (Sr) 1b(Ti) 3c(O)	(0,0,0) (0.5,0.5,0.5) (0.5,0.5,0)	1 1 1	00-035-0734

5.3 Results

5.3.1 Electron diffraction and diffraction contrast imaging

Diffraction contrast image of the $Li(Ni, Mn)_xO_y$ thin film on 111 single crystal Nb:STO substrate is given in figure 5.2a. The film is ~350-400 nm in thickness. The top most surface of the film is almost smooth and uniform without any significant undulations or roughness.

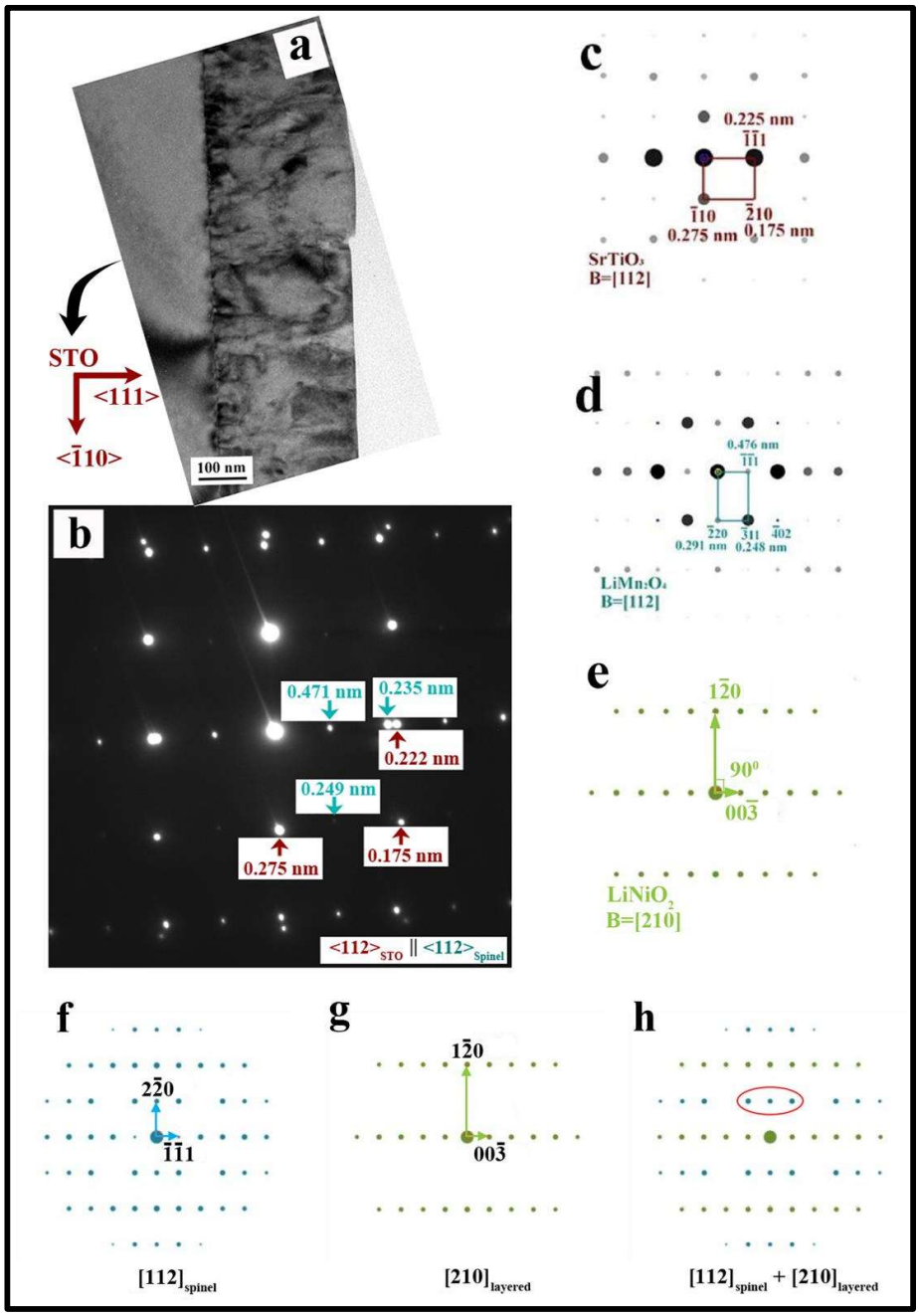

Figure 5.2: ***(a)*** *Cross-sectional TEM bright-field image of the combinatorially deposited $Li(Ni, Mn)_xO_y$ (LNMO) thin film on 111 single-crystal Nb-doped $SrTiO_3$ (Nb:STO) substrate (aligned with the experimental diffraction pattern in figure 5.2b. 110 and 111 directions are also marked in the image. 111 is the film growth direction and 110 is parallel to the interface).* ***(b)*** *Electron diffraction pattern from the thin film and the substrate. The substrate is oriented along B= [112] zone axis.* ***(c-e)*** *Simulated electron diffraction*

patterns of cubic $SrTiO_3$, cubic $LiMn_2O_4$ spinel (LMO) and rhombohedral layered $LiNiO_2$ (LNO) along B= [112], [112], and [210] zone axis respectively. Simulated electron diffraction pattern from ***(f)*** *cubic $LiMn_2O_4$ spinel from B = [112],* ***(g)*** *rhombohedral layered $LiNiO_2$ along B = [210] and,* ***(h)*** *simulated composite electron diffraction pattern from [112] zone axis of cubic $LiMn_2O_4$ spinel and [210] zone axis of rhombohedral layered $LiNiO_2$ phase. The blue spots encircled in red represents the unique diffraction spots from spinel for confirmative substantiation of the presence of the spinel phase. Experimentally observed d-spacings are marked on the experimental diffraction pattern. Theoretically expected d-spacings and orientation of reciprocal lattice vectors are marked on the simulated diffraction patterns. Simulated diffraction patterns are not to scale with the experimental diffraction pattern.*

In few regions some inclined depressions can be seen. In the thin film, grain boundary contrast is not distinctly visible. However, regions of dark contrast are observed in the film with darker regions concentrating more towards the film/substrate interface. Apart from local composition fluctuations, localized thickness variations resulting in the change of diffraction conditions might have generated this distributed dark and bright contrast all across the film surface. The substrate was aligned to the nearest zone axis in order to make the interface parallel to the electron beam. The interface between the film and the STO substrate is sharp and clearly defined. Bend contours are observed in the substrate, which indicates that the substrate is quite thin and the set of diffracting planes are not parallel everywhere due to the rotation and bending of planes in that region. A distributed dark contrast is observed at the film-substrate interface. In diffraction contrast images such dark contrast generally appears due to strain localization as a consequence of mismatch in the constituent lattices. However, it has to be confirmed through tilt experiment. Be it at the interface or at the film no dislocation or any other planar defect is observed. Analysis of dislocation density or planar defects is not the primary focus of this chapter. While doing the imaging and diffraction experiments in order to understand the phase evolution, high

density of dislocation or planar faults could not be seen. Based on this observation, it can be inferred that defect density at the interface and in the film is pretty low.

In order to understand phase evolution in the film and its epitaxial relationship with the substrate, the substrate was tilted to the nearest zone axis and the interface was kept almost edge-on while recording the diffraction pattern from the film and the substrate. The diffraction pattern shown in figure 5.2b has been obtained from the film/substrate interface. The diffraction pattern has been aligned with respect to the image in figure 5.2a. The diffraction pattern was recorded with a ~20 micrometer diameter SAD aperture, which allows the diffraction to occur from the substrate and the film. The obtained diffraction pattern appears to have arisen from crystalline phases as all spots are quite sharp and intense. The epitaxy could also be seen with small spots appearing symmetrical to the bigger spots. Since the deposition is done by PLD process, the grains get sufficient time to relax their strain. This in turn, gives bigger grain size, which is reflected in the sharpness of the diffraction pattern in figure 5.2b. The experimentally measured d-spacings are marked on the pattern. Such d-spacings seem to be deviating from the reported data, as the stoichiometry in the synthesized material might have changed. Although the diffraction spots arising from STO substrate could be distinguished, other spots could be associated either with cubic $LiMn_2O_4$ spinel or rhombohedral $LiNiO_2$ layered structure. As reported in earlier literature, monoclinic Li_2MnO_3 phase also may be present. However, in the present situation no distinguishable diffraction signature from this phase could be discerned. This necessarily means the phase may not be present in the film. In order to index the diffraction pattern unambiguously, diffraction pattern from cubic STO along [112], cubic $LiMn_2O_4$ along [112] and rhombohedral layered $LiNiO_2$ along [210] were simulated and they are given in figure 5.2(c-e) respectively.

It appears from the simulated diffraction pattern of STO along [112] that almost equall intense $(\bar{1}\bar{1}1)$ and $(\bar{1}10)$ spots appear at right angle to each other and intensity of the $(\bar{2}01)$ spot is relatively weak. The d-spacings are 0.225 nm, 0.275 nm and 0.175 nm respectively. The orientation and d-spacings match quite closely with the experimental diffraction pattern. It can be concluded from this observation that the STO substrate is oriented along [112] zone axis. According to the simulated pattern the $(\bar{1}\bar{1}1)$ spot should be most intense, the $(\bar{1}10)$ spot should be less intense and $(\bar{2}01)$ spot should be even less intense. However, in the experimental pattern all the three spots are almost equally intense. This could be due to the superposition of some reflections from the thin film and the variation in sample thickness. Additionally, the Nb:STO substrate was tilted to the [112] zone axis as close as possible keeping the interface edge-on without losing the diffraction spots from the film. All the above mentioned factors in addition to the wedge shape of the sample may be accounted for the variation in the intensity of the diffraction spots. The asymmetric unit of cubic $LiMn_2O_4$ spinel is rectangular (Figure 5.2d) and $(\bar{1}\bar{1}1)$, $(\bar{2}20)$ and $(\bar{3}11)$ spots should be present. The d-spacings corresponding to $(\bar{1}\bar{1}1)$, $(\bar{2}20)$ and $(\bar{3}11)$ reciprocal lattice vectors are 0.476 nm, 0.291 nm and 0.248 nm respectively. The intensity of the $(\bar{3}11)$ spot is stronger and the intensity for other two spots is relatively weaker. In the experimental pattern, an intense spot at 0.471 nm is observed and the spot at 0.249 nm is quite weak. The spot at 0.291 nm is not seen. It might be due to the fact that spinel phase is not oriented favorably along [112] zone axis due to the wedge shape of the sample. The variation in intensity can be explained by the superposition of some of the reflections from the rhombohedral $LiNiO_2$ phase that may be present in the film. As the $(\bar{2}20)$ spot of spinel

(0.291 nm) is located close to that of $(\bar{1}10)$ spot of Nb:STO (0.275 nm), it might not be possible to identify such a reflection distinctly. However, it is clear that the spinel phase is present in the film. It is further observed that the $(\bar{1}\bar{1}1)$ reciprocal lattice vector of spinel is parallel to $(\bar{1}\bar{1}1)$ vector of Nb:STO. The orientation relationship between Nb:STO and cubic $LiMn_2O_4$ spinel are $[112]_{STO}\|[112]_{Spinel}$ and $(\bar{1}\bar{1}1)_{STO}\|(\bar{1}\bar{1}1)_{Spinel}$. The simulated diffraction pattern of rhombohedral $LiNiO_2$ along [210] is given in figure 5.2e. The asymmetric unit cell of this phase along this zone axis is a parallelogram with almost equally intense $(00\bar{3})$, $(1\bar{2}0)$ and $(1\bar{2}\bar{3})$ spots at the corners. So the $(00\bar{3})$ type spot from rhombohedral layered $LiNiO_2$ should superimpose on $(\bar{1}\bar{1}1)$ reflection of cubic $LiMn_2O_4$ spinel. This explains the relatively higher intensity that of such spot. Additionally, the $(1\bar{2}0)$ spot of layered rhombohedral $LiNiO_2$ should superimpose with the $(4\bar{4}0)$ spot of cubic $LiMn_2O_4$ spinel. All other diffraction spots of layered rhombohedral $LiNiO_2$ from [210] zone axis should superimpose with the diffraction spots from [112] zone axis of cubic $LiMn_2O_4$ spinel phase. Individual simulated diffraction patterns from the [112] zone axis of cubic $LiMn_2O_4$ spinel, [210] zone axis of layered rhombohedral $LiNiO_2$ phase and their superimposition pattern are given in figure 5.2(f-h). It is observed from such a superimposed pattern that the presence of the cubic $LiMn_2O_4$ spinel phase can be confirmed unambiguously from the spots circled in red in figure 5.2h. These spots are present in the experimental diffraction pattern (Figure 5.2b). However, all the diffraction spots from the [210] zone axis of layered rhombohedral $LiNiO_2$ are coincident with the cubic $LiMn_2O_4$ spinel phase. So, the presence of layered rhombohedral $LiNiO_2$ phase cannot be confirmed unambiguously through this diffraction experiment. However, there is a good possibility that the layered rhombohedral

$LiNiO_2$ phase is present in the film. Should this phase be present in the film, then the orientation relationship should have been $[112]_{spinel}||[210]_{layered}$ and $[\bar{1}\bar{1}1]_{spinel}||[00\bar{3}]_{layered}$. Dark field imaging with the spots as encircled in figure 5.2h could prove the presence of the spinel phase.

In order to distinguish between the cubic $LiMn_2O_4$ spinel phase and the rhombohedral layered $LiNiO_2$ phase tilting experiment was carried out. The experimentally observed diffraction patterns along with the simulated ones for cubic $LiMn_2O_4$ spinel phase as well as that of rhombohedral layered $LiNiO_2$ phase along different zone axes are given in figure 5.3. Stereographic projection of $LiMn_2O_4$ spinel phase and the rhombohedral layered $LiNiO_2$ phase indicates that tilting around the 220 spot of spinel is not quite useful as any major zone axis for $LiNiO_2$ is quite far off in terms of angular orientation. So the diffraction patterns are mixed with spinel pattern and some random diffraction spots from layered $LiNiO_2$. These types of patterns are not quite useful to substantiate the presence or absence of any phase unambiguously. However, tilting around the 003 spot of layered $LiNiO_2$ or 111 spot of spinel takes both the phase through a number of zone axes. The series of zone axes patterns in figure 5.3 were obtained by tilting around 003 spot of layered $LiNiO_2$ or 111 spot of cubic $LiMn_2O_4$ spinel. Starting from the [112] zone axis of cubic $LiMn_2O_4$ spinel or the [210] zone axis of rhombohedral layered $LiNiO_2$ phase the orientation relationship can be explained easily. The simulated [112] zone axis pattern from the cubic $LiMn_2O_4$ spinel phase matches exactly with the experimental pattern. Similar match for rhombohedral layered $LiNiO_2$ structure were found when viewed along the [210] zone axis. The ratio between two principal vectors (g_1 and g_2) in the diffraction pattern (Figure 5.3) also matches exactly and it is ~1.63 and confirms the experimental observation.

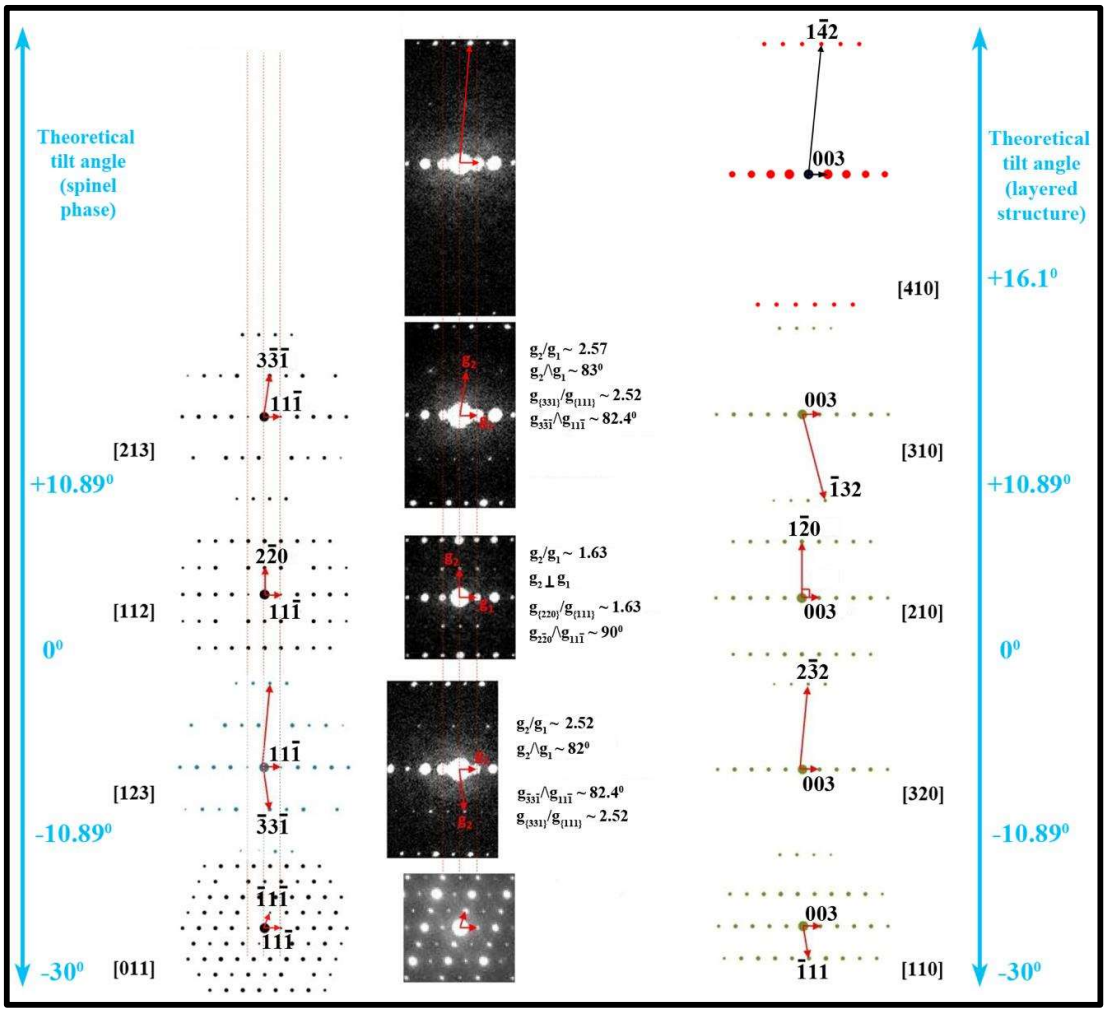

Figure 5.3: *Experimentally observed tilt series diffraction patterns from the thin film around the $\bar{1}\bar{1}1$ reciprocal lattice vector of cubic $LiMn_2O_4$ spinel (LMO) or $00\bar{3}$ reciprocal lattice vector of rhombohedral layered $LiNiO_2$ (LNO). Simulated diffraction patterns for cubic $LiMn_2O_4$ spinel and rhombohedral layered $LiNiO_2$ along with the orientation of the reciprocal lattice vectors are given for each zone axis. The simulated patterns are to the scale with the experimental patterns. Tilt angles and the ratio of two principal vectors in the diffraction pattern are given.*

Tilting +10.9⁰ about $11\bar{1}$ axis of cubic $LiMn_2O_4$ spinel or 003 axis of rhombohedral layered $LiNiO_2$ phase, a new zone axis is arrived at, which matches with the [213] zone axis of cubic $LiMn_2O_4$ spinel phase or the [310] zone axis of the rhombohedral layered $LiNiO_2$

phase. The ratio of the two principal vectors (g_1 and g_2) in the experimental pattern (Figure 5.3) matches with the same ratio in the simulated pattern for both the phases, which is equal to ~2.57 for both the phases. Further tilting by 16.1° about the 003 reciprocal lattice vector of rhombohedral layered $LiNiO_2$ phase, a new zone axis is arrived at, which matches with the [410] zone axis pattern of the layered $LiNiO_2$ phase. Tilting -10.9° about $11\bar{1}$ reciprocal lattice vector of cubic $LiMn_2O_4$ spinel phase or the 003 reciprocal lattice vector of the rhombohedral layered $LiNiO_2$ phase, a new zone pattern is arrived at. The zone axis pattern matches with the simulated [123] pattern of cubic $LiMn_2O_4$ spinel or the simulated [320] zone axis pattern of rhombohedral $LiNiO_2$ phase. The experimentally observed ratio of the principal reciprocal lattice vectors (Figure 5.3), which is ~2.52, matches with both the simulated patterns. Further tilting to -30° leads to another zone axis pattern, which matches with the simulated [011] pattern of the cubic $LiMn_2O_4$ spinel and the simulated [110] zone axis pattern of the rhombohedral layered $LiNiO_2$ phase. The experimentally observed ratios of the principal reciprocal lattice vectors also match with the simulated patterns. From the above tilt experiments, it can be concluded that the presence of rhombohedral layered $LiNiO_2$ phase cannot be confirmed with certainty as this phase is completely indistinguishable from the cubic $LiMn_2O_4$ spinel phase in the reciprocal space. In order to distinguish them clearly high resolution imaging should be resorted to (cf. section 5.3.3). However, grain boundary contrast is not observed in the thin film. Although, the cubic $LiMn_2O_4$ spinel phase and the rhombohedral $LiNiO_2$ phase are quite different crystallographically, they are very similar in the reciprocal space owing to similar d-spacings of many of the reflections.

5.3.2 Spectral imaging and composition analysis

HAADF image of the thin film and the substrate is given in figure 5.4a and its zoom-in version is given in figure 5.4b. The film is ~350-400 nm thick that can again be confirmed from the image. The interface between the thin film and the substrate is quite sharp with distributed black contrast along it as observed in figure 5.4b. The sharp interface is not observed in figure 5.4a as the sample is tilted by ~13^0 towards the detector. A few dark contrast regions are observed near the upper part of the film in figure 5.4a, whereas in both the images a distinct white contrast is observed near the interface. The presence of dark regions in the upper part of the film may be attributed to the localized bending and presence of lighter elements in the top part. Whereas, the continuous bright contrast near the interface may represent the presence of heavier elements near the interface. As the atomic number of Ni (Z= 28) is more than that of Mn (Z= 25), it can be concluded that the near interface region is Ni-rich. The thickness of which is ~60 nm. The spectral map from the image in figure 5.4c indicates that the near interface region is Ni-rich and almost no Mn is present. Away from the interface Ni and Mn concentration becomes almost equal. From the spectral map, cross diffusion of Ni or Mn into the substrate or Sr and Ti into the film could not be observed. XEDS line scan profile of Ni, Mn, Sr and Ti is given in figure 5.4c. The line scanning was done along the line marked in figure 5.4a. It appears from the line scan profile that Ni and Mn concentration is almost similar from the surface to the interior of the film. Only near the interface Mn concentration drops gradually and the Ni concentration picks up. From the interface Ni concentration gradually drops, and Sr and Ti signal picks up. It is expected that the Ni signal should drop abruptly at the interface, and the Sr and the Ti signal should pick up sharply. As the sample is tilted, the interface is not edge-on. So the signal drops gradually.

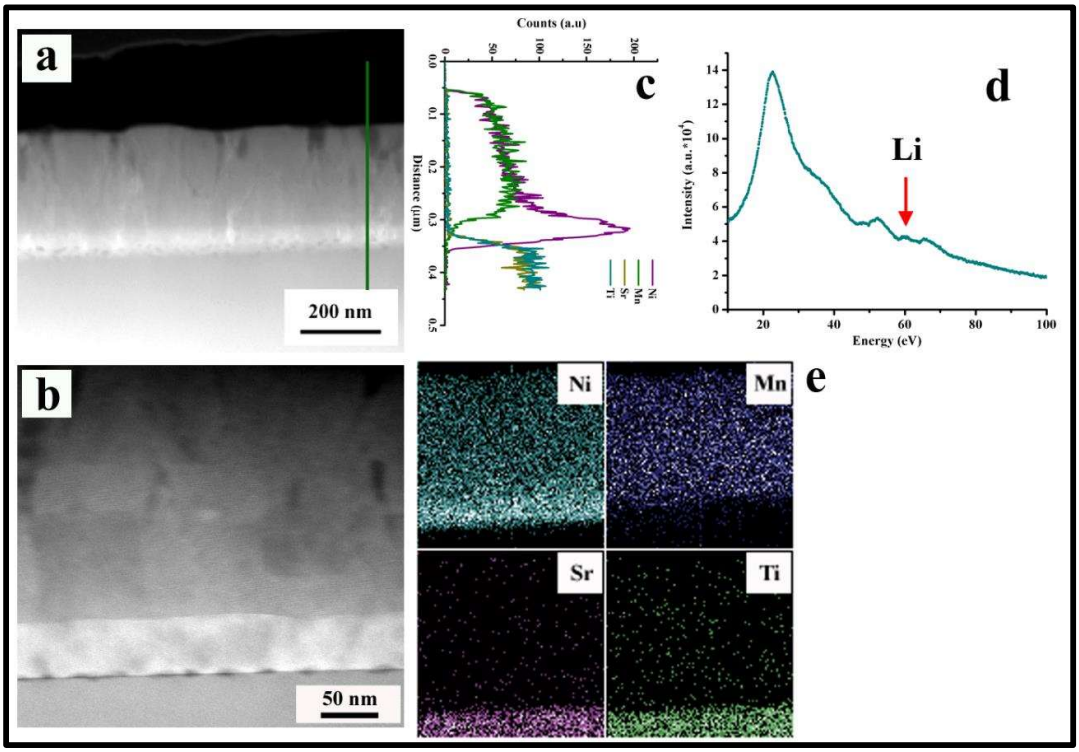

Figure 5.4: ***(a)*** *HAADF image from the thin film and the substrate,* ***(b)*** *Magnified HAADF image of the thin film and the substrate and* ***(e)*** *the XEDS map of Ni, Mn, Sr and Ti from the thin film and the substrate.* ***(c)*** *XEDS line scan of the constituent elements along the line marked in* ***(a)****,* ***(d)*** *Low-loss EELS spectra from the thin film obtained in diffraction-coupled mode.*

It is important to point out that the line scan is not perpendicular to the interface. The line scan in figure 5.4c has not been corrected for perpendicularity. It just shows the variation in the elemental profiles along the line marked in figure 5.4a. The EELS spectra from the film is given in figure 5.4d. The energy loss edge at ~55 eV indicates that Li is present in the film. It is the only spectroscopic signature that could be obtained from the film. The STEM-EDS mapping in figure 5.4e represents the spatial distribution of elements in the thin film. It has been observed from the elemental map that Sr and Ti are homogeneously distributed all across the substrate. The presence of Ni-rich region within the film near the interface region has been observed in figure 5.4b (white color band). Both Mn and Ni have

been found to be homogeneously distributed just above the Ni-rich region in the thin film. Moreover, there is no indication of any significant composition fluctuation in the bulk of the film other than Ni-rich region. It can be concluded that the film is predominantly Ni-rich near the interface and the interface between the substrate and the film is chemically sharp. The deposition schedule adopted in the present study produces a core-shell structure where the core is ~60 nm thick and Ni rich. The shell region is almost homogeneous in terms of Ni and Mn distribution. Li is also present in the film. This further indicates that the deposition rate of Mn and Ni are not similar. Due to the lower deposition rate of Mn, the core is Ni-rich.

5.3.3 Structural imaging and interfaces

High-resolution image from the film-substrate interface, center and top of the film along with a representative FFT are given in figure 5.5(a-d). In the image from the interface (Figure 5.5a), cross fringe pattern from the Nb:STO substrate can be observed. In the film region, fringe contrast with 0.230 nm spacing and parallel to the interface could be observed. This spacing matches quite closely with the (222) spacing of cubic $LiMn_2O_4$ spinel phase or (006) spacing of rhombohedral $LiNiO_2$ phase. Just at the interface, the fringes are locally bent which indicates the presence of residual strain at the film/substrate interface. Presence of such residual strain generates the dark contrast at the interface as seen in figures 5.2a and 5.4b. Higher degree of distortion along the interface within ~6 nm distance towards the film has been observed. This may be due to the presence of strain and misfit dislocations near the interface region. Beyond this region the crystallinity and uniformity in the fringes have improved.

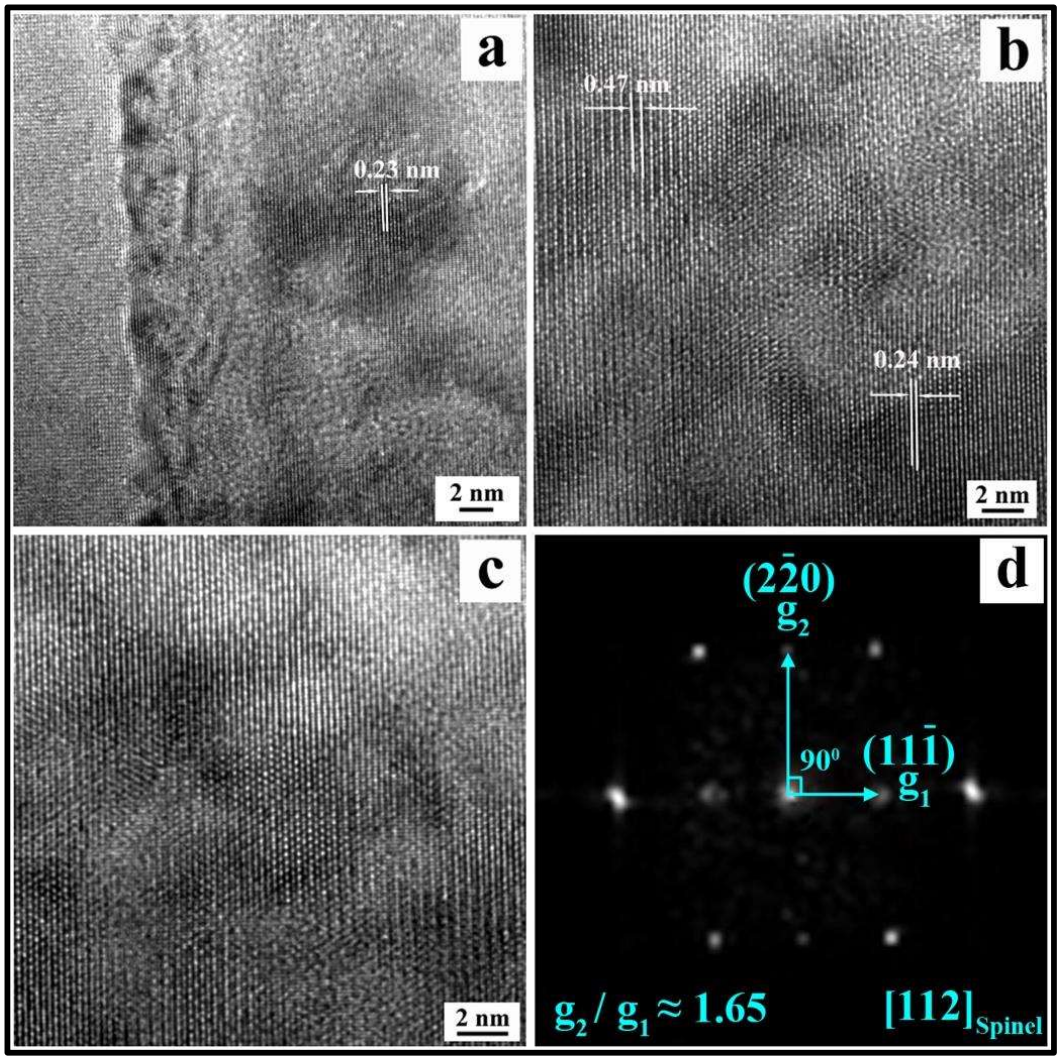

Figure 5.5: *High resolution phase contrast image from* ***(a)*** *thin film and substrate interface* ***(b)*** *central region of the thin film and* ***(c)*** *top region of the thin film. Nb-doped $SrTiO_3$ (Nb:STO) substrate was oriented along B=[112] zone axis while imaging* ***(d)*** *FFT from the image in* ***(c)****, which confirms the presence of the cubic $LiMn_2O_4$ phase in the film.*

From the central region of the thin film as shown in figure 5.5b, similar parallel fringes with 0.240 nm spacing could be observed. The overall contrast in this central part of the high-resolution image has increased with individually resolved atomic columns in some of the regions. However, in some localized areas, alternate fringe contrast becomes very weak or it is almost absent. As a result, the fringe spacing becomes 0.470 nm which matches with

the 111 spacing of cubic $LiMn_2O_4$ spinel phase or with the 003 spacing of rhombohedral layered $LiNiO_2$ phase. Alternate fringes may become weaker due to the ordering of any of the transition metals in the host lattice of metal oxide. Such fringes may also become weaker in contrast due to change in thickness of the sample which is not quite expected over a length scale of ~5-6 nm. Otherwise it could happen due to some localized structural changes, which is not easy to understand and explain due to the mechanism of contrast formation in phase contrast imaging. Sample preparation artefacts may also bring about such changes. Extreme care was taken to alleviate such kind of artefact generation and it has been discussed in the experimental section.

From the top region of the film (Figure 5.5c), similar parallel fringes with same spacing could be observed with more improved contrast and much resolved atomic column contrast than central part. However, distinct contrast variation over a particular fringe is noticed. Although these high-resolution images were taken at same defocus value, still it is seen that over a particular fringe, in certain regions bright atom column like contrast is obtained and in certain regions on the same fringe that atom column like contrast is lost. This may be due to the thickness variation or distinct orientation of domains in the specimen across these regions. In addition to this, the difference in the inner mean potential of the individual elements also changes its contrast transfer function due to which at the same thickness the contrast may vary depending on the chemistry of individual atomic columns. However, white and black contrast of the same atomic column depends on the sign of the contrast transfer function (CTF) with respect to its spatial frequency. If CTF is positive, the atomic columns appear white whereas if CTF is negative atomic columns look black. All these localized contrast variations could be due to some structural changes which is not direct and easy to explain. However, effect of microscope parameters could not be ruled out. In

order to understand the contrast and associate it with the structural changes while gradually moving from the interface towards the film surface, better understanding of the structure and the imaging parameters are required.

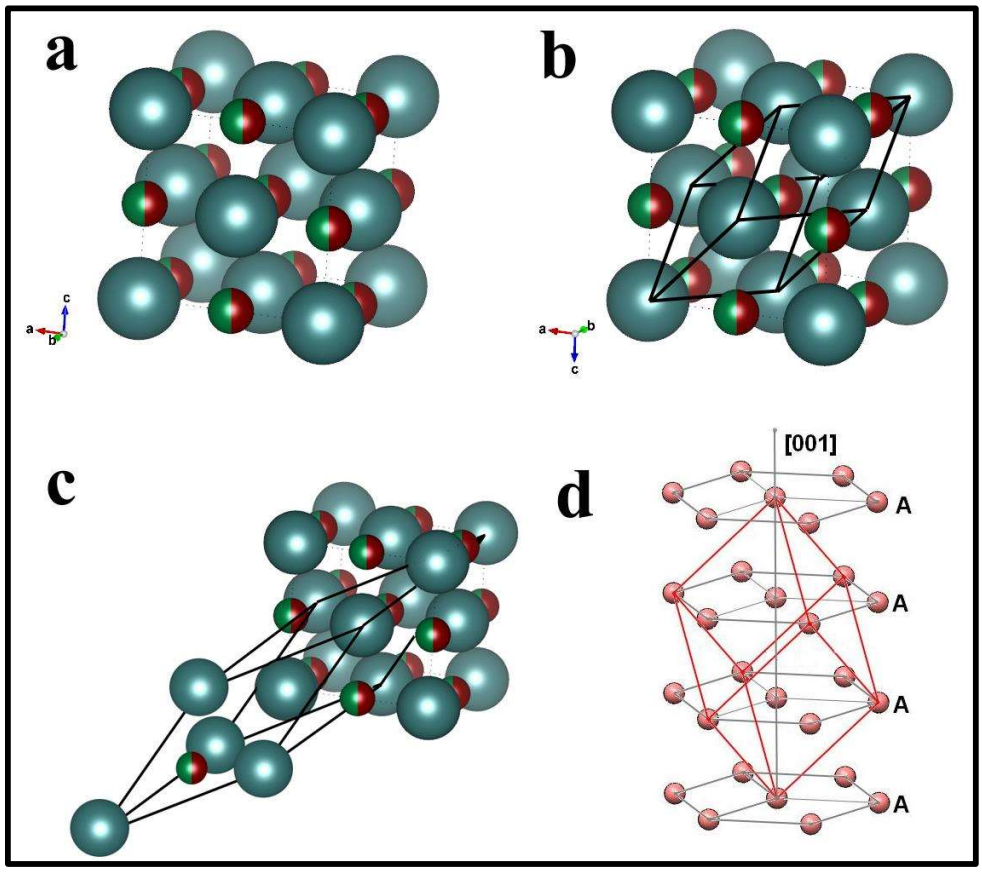

Figure 5.6: *Schematic representation of* ***(a)*** *cubic rock-salt structure* ***(b-c)*** *distortion of cubic rock-salt structure leading to rhombohedral symmetry* ***(d)*** *hexagonal representation of rhombohedral lattice.*

From the high-resolution images, it is not possible to confirm the presence or the absence of the spinel or the rhombohedral layered phases. With so many parameters like defocus, thickness, change in chemistry etc., playing its own role, quantitative understanding of the images is not possible. However, a representative FFT (Figures 5.5b and 5.5c) is given in figure 5.5d. The FFT matches well with the [112] zone axis pattern of the cubic $LiMn_2O_4$

spinel phase. The ratio of the two principal lattice vectors is ~1.65, which is close to the theoretical value (Figure 5.3). However, the ratio of the principal lattice vectors for the rhombohedral layered $LiNiO_2$ phase when viewed along the [210] zone axis is ~3.3. Such a ratio in the FFT (Figures 5.5b and 5.5c) is not seen. Therefore, the presence of the rhombohedral layered phase cannot also be confirmed from this observation.

Rhombohedral $LiNiO_2$ is considered to be a derivative of rock-salt structure. In rock-salt structure Cl^--ions occupy the corners and face centers of the cubic lattice and the Na^+-ions completely fill the octahedral sites. However, in a rock-salt structure when Cl^--ions are replaced by oxygen ions and Na^+-ions are replaced by Li^+ and Ni^{3+} ions, disordered $LiNiO_2$ structure results (Figure 5.6a). Ideally, $LiNiO_2$ is cation ordered. As a result, Li^+-ions and Ni^{3+}-ions are present in alternate layers. Owing to the difference in the cation sizes the cubic structure undergoes distortion. Distortions along the cube edge or along the body diagonal lead to the formation of tetragonal or rhombohedral structures respectively. While, the cubic to tetragonal transformation is understood with relative ease, the cubic to rhombohedral transformation is best appreciated by model. A rock-salt structure with minimal distortion can be seen as a rhombohedral structure with one formula unit instead of four formula units as in the case of a cube (Figure 5.6b). The lattice parameter of this rhombohedral structure is $a/\sqrt{2}$, where 'a' is the lattice parameter of the cube and $\alpha=60^{o}$. In a more distorted structure, the rhombohedral lattice is represented by two formula units instead of four formula units of cubic lattice (Figure 5.6c). In this distortion, the lattice parameter of the rhombohedral cell is $\sqrt{3}a/\sqrt{2}$ where 'a' is the lattice parameter of the cube and $\alpha= 33^{0}34'$. Depending on the extent of distortion, the value of 'α' changes. Rhombohedral $LiNiO_2$ assumes this structure. However, this rhombohedral structure could equivalently be represented as a hexagonal lattice (Figure 5.6d), where body diagonal of

the distorted rhombohedral cell is equal to the c-axis of the hexagonal cell. Cubic $LiMn_2O_4$ structure, although contains a large number of ions, it does not undergo any distortion and retains cubic symmetry. The ionic arrangement in this structure can be explained by stacking 2X2X2 cubic unit cell, in which corners and face centers of each unit cell is occupied by oxygen ions, half of the octahedral voids are occupied by manganese ions and $1/8^{th}$ of the tetrahedral voids are occupied by lithium ions. In terms of void filling, the basic difference between rhombohedral $LiNiO_2$ structure and cubic $LiMn_2O_4$ spinel structure is that in case of spinel structure half the octahedral voids are filled in contrast to complete occupancy of the octahedral voids in $LiNiO_2$ structure.

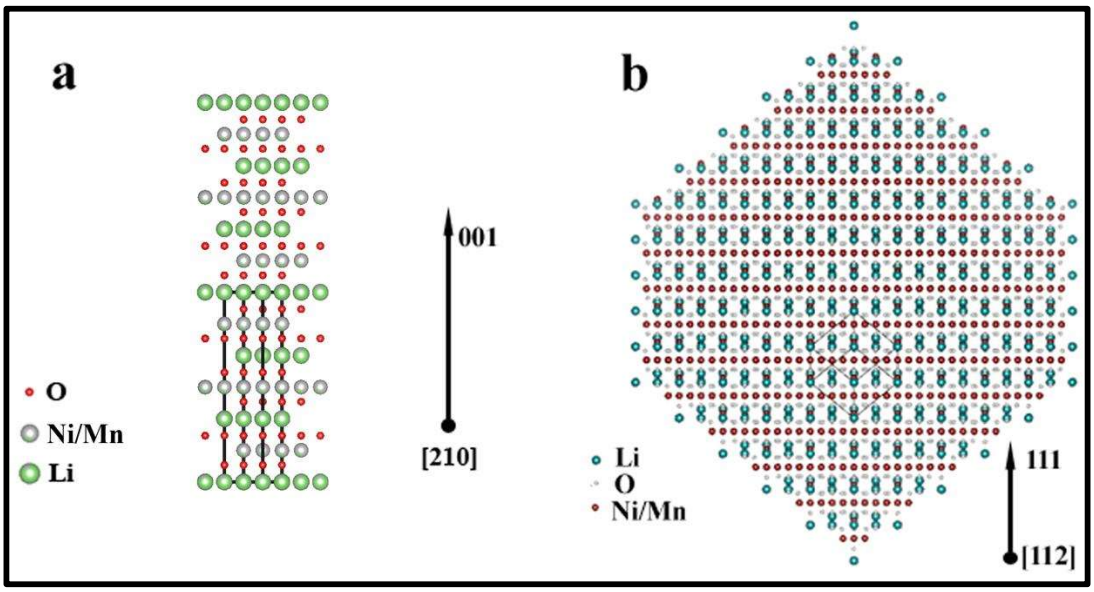

Figure 5.7: *Projection diagram of* ***(a)*** *rhombohedral layered $LiNiO_2$ (LNO) which is projected along [210] with 001 upward vector and* ***(b)*** *cubic $LiMn_2O_4$ spinel (LMO) which is projected along [112] with 111 upward vector.*

The projection of rhombohedral ($\alpha = 33^0 34'$) $LiNiO_2$ along [210] and cubic $LiMn_2O_4$ spinel along [112] are given in figure 5.7(a-b). From the projection diagram of the $LiNiO_2$ phase, it is clearly observed that sequential stacking of Ni-ion layer, oxygen-ion layer and Li-ion layer along the [001] direction builds up the structure. The separation between two

consecutive Ni-ion layers is 0.470 nm which is equivalent to 003 planar spacing of $LiNiO_2$ and in between two Ni-ion layers one Li-ion layer is located. The spacing between one Ni-ion layer and one Li-ion layer is 0.240 nm which is equivalent of 006 planar spacing of $LiNiO_2$. Similarly, from the projection diagram of cubic $LiMn_2O_4$ spinel phase (Figure 5.7b) along [112] direction, it is clearly observed that this is also a layered structure.

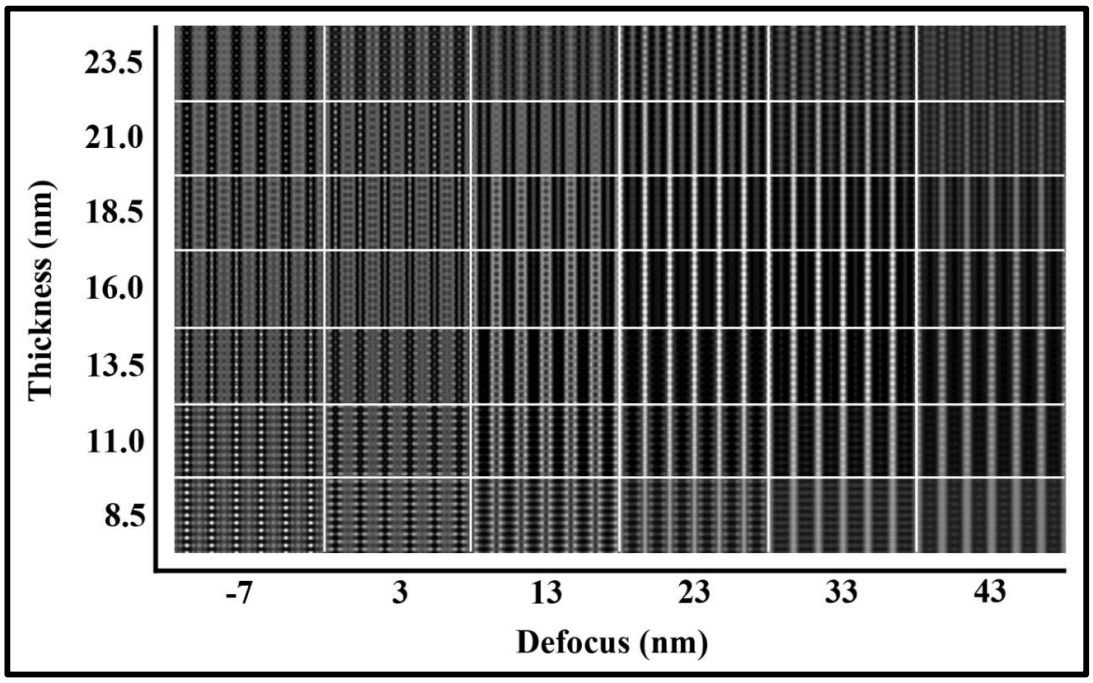

Figure 5.8: *Simulated Defocus-Thickness map of rhombohedral layered $LiNiO_2$ (LNO) along [210] by multislice technique. The simulation parameters are C_s= (-0.00683) mm, A1=0.7246 nm, A2=46.68 nm, B2=13.8 nm, A3=295.3 nm, S3=90.35 nm. In the region of interest (Defocus~23-33nm and thickness~ 18-21nm) alternating bright and faint fringes are observed. Faint fringes are supposed to be from Li-layer and the relatively bright fringes are from Ni/Mn ions. The oxygen layers are not imaged.*

However, all the layers are not chemically equivalent. One observes layers with Mn-ion only, whereas some of the Mn-ion layers are mixed with oxygen and the Li-ions. The separation between a pure Mn-ion layer with that of the mixed one is 0.24 nm. This is equivalent to 222 planar spacing of cubic $LiMn_2O_4$ structure. It is worth-mentioning that

the separation between two consecutive Mn-ions in the chemically impure layer is just double than the same spacing in the chemically pure layer. This is a distinguishing feature with rhombohedral $LiNiO_2$ where the spacing between two consecutive Ni-ions in the same layer is same in all the layers. Moreover, it is important to note that Ni and Mn should replace each other in the lattice in a thin film of $Li(Ni, Mn)_xO_y$ composition. A sound interpretation of variation in contrast of high-resolution image is necessary in order to correlate the image with the projected structures.

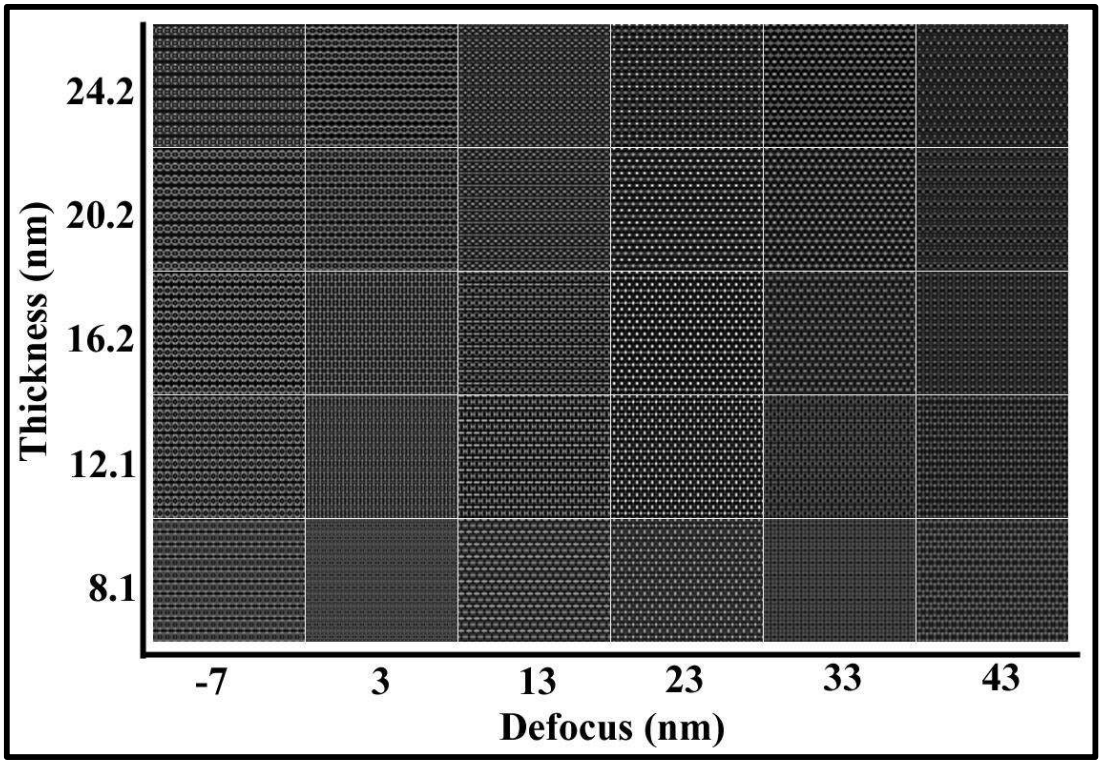

Figure 5.9: *Simulated Defocus-Thickness map of cubic $LiMn_2O_4$ spinel (LMO) along [112] by multislice technique. The simulation parameters are C_s= (-0.00683) mm, A1=0.7246 nm, A2=46.68 nm, B2=13.8 nm, A3=295.3 nm, S3=90.35 nm. For this structure from this zone axis, the atom columns are mostly having mixed chemistry.*

The simulated defocus-thickness map of negative-aberration corrected high-resolution phase contrast images for the rhombohedral $LiNiO_2$ phase along [210] is given in figure 5.8. The fringe pattern that is observed in the defocus-thickness map corresponds to 003 or 006 planes of rhombohedral $LiNiO_2$ layered structure. The exercise was done over a wide range of third-order coefficient of spherical aberration. The result indicates that with negative aberration coefficient, Ni-layers and Li-layers could be imaged over a workable range of defocus and thickness. With C_s=-0.00683 mm, over a defocus range of 23-33 nm, it is possible to image Ni and the Li layers simultaneously over a thickness range of 8-20 nm. However, appearance of the individual layers varies with thickness. It has been observed from the defocus – thickness map that at higher thickness values within the defocus range shown, the appearance of 003 planes is dominant with hardly any contrast from 006 planes. The contrast from the Li-layer is generally less bright and the individual atom columns are not resolved. The contrast from the Ni-layers is brighter than the Li-layers and often individual atom columns are resolved. However, the width of the Ni-layers changes over defocus and thickness, which is partially due to the appearance of oxygen layer. Simulated defocus-thickness map of negative aberration corrected phase contrast images for cubic $LiMn_2O_4$ spinel structure along [112] is given in figure 5.9. As discussed earlier, in this structure chemically pure oxygen and Li-layers are not seen from this direction. However, chemically pure and chemically impure Ni layers are imaged in the defocus range of 13-33 nm over 8-20 nm thickness. With 23 nm defocus, over a thickness range of 8-24 nm, it is seen that pure Mn layer is present in addition to Ni/O layer atoms stacked along [111]. With 13 nm defocus, over 12-16 nm thickness both the layers are imaged. With 33 nm defocus, over 20-24 nm thickness both the layers are imaged. It is

worth-mentioning that difference in spacing between two consecutive Ni-ions in the chemically impure layer is distinguishable.

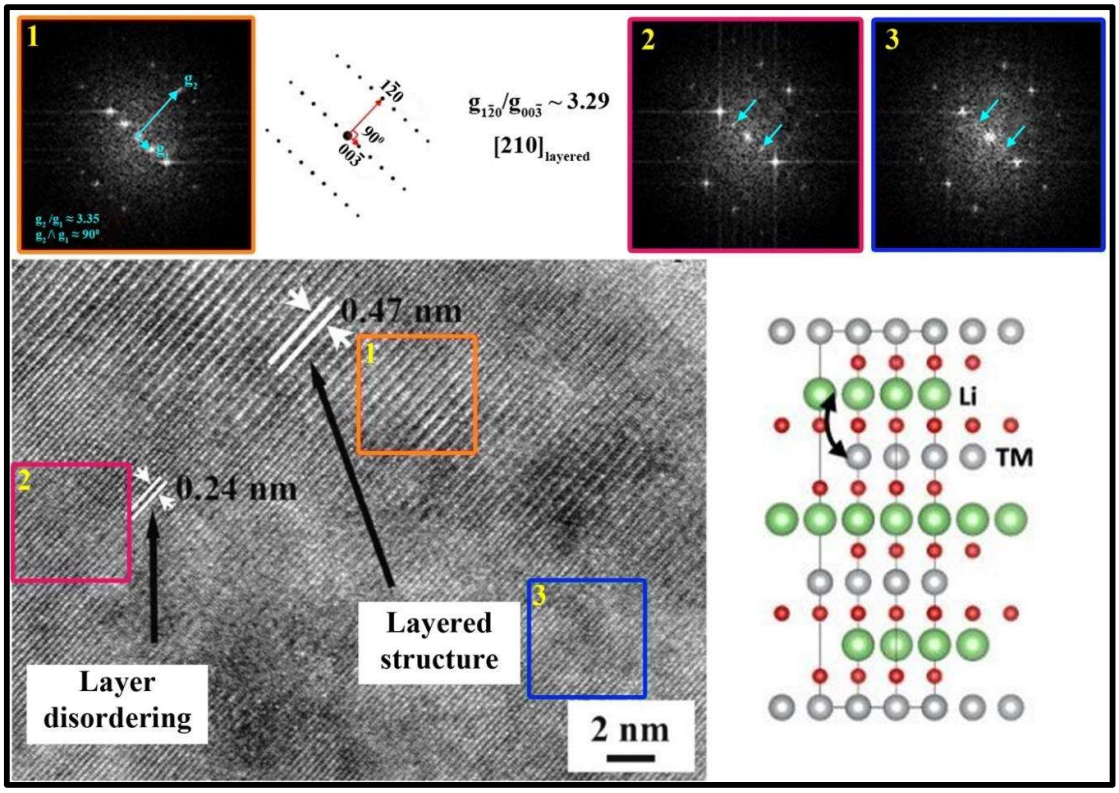

Figure 5.10: *Negative aberration-corrected high resolution phase contrast image of $Li(Ni,Mn)_xO_y$ thin film in which ordered and disordered regions of rhombohedral layered $Li(Ni, Mn)O_2$ regions and the coherent interface between them are observed. Regions are marked as 'Layered structure' and 'Layer disordering'. Experimental correction parameters are C_s= (-0.00683) mm, A1=0.7246 nm, A2=46.68 nm, B2=13.8 nm, A3=295.3 nm, S3=90.35 nm. FFTs from the regions '1', '2' and '3' marked by orange, pink and blue windows respectively are given in 'FFT1', 'FFT2' and 'FFT3'. The simulated diffraction pattern from rhombohedral layered $LiNiO_2$ along B=[210] is given by the side of the FFT1. The two dimensional projection of the same structure along B=[210] is given below the FFT2 and FFT3. FFT1 shows complete ordering in rhombohedral layered $Li(Ni, Mn)O_2$, FFT2 shows weak ordering and the FFT3 shows almost no ordering in the same structure.*

Negative-aberration corrected high-resolution phase contrast image from the film is given in figure 5.10. In the image parallel fringes with spacing of 0.240 nm could be observed. The contrast from both the fringes is almost similar. However, in certain locations, fringes with 0.470 nm spacing are observed and in between two fringes very weak contrast is observable.

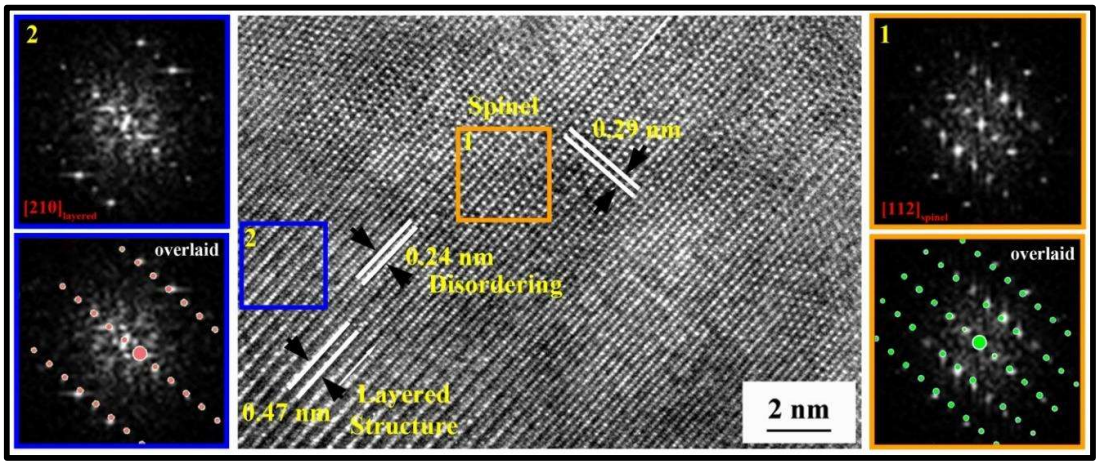

Figure 5.11: *Negative aberration-corrected high resolution phase contrast image of Li(Ni, Mn)$_x$O$_y$ thin film in which cubic Li(Ni, Mn)$_2$O$_4$ spinel and rhombohedral layered Li(Ni, Mn)O$_2$ regions and the coherent interface between them are observed. Experimental correction parameters are C_s= (-0.00683) mm, A1=0.7246 nm, A2=46.68 nm, B2=13.8 nm, A3=295.3 nm, S3=90.35 nm. FFTs from region '1' and region '2' as marked by orange and blue windows are given as FFT1 and FFT2. The corresponding simulated diffraction patterns overlaid on the FFTs are given just below them. Region '1' matches with cubic LiMn$_2$O$_4$ spinel along B=[112] and region '2' matches with rhombohedral layered LiNiO$_2$ along B=[210].*

The 0.240 nm spacing is equivalent to 006 spacing of rhombohedral $LiNiO_2$ or 222 spacing of cubic $LiMn_2O_4$ spinel. The 0.470 nm spacing is equivalent to 003 spacing of rhombohedral $LiNiO_2$ or 111 spacing of cubic $LiMn_2O_4$ spinel. The image was recorded with C_s= -0.00683 mm and with ~23 nm defocus. Under this condition, Ni-layer and the Li-layer both should be imaged. However, contrast from the Li-layer should be weaker.

The region with 0.240 nm spacing and with almost similar contrast represents disordered region of rhombohedral layered $LiNiO_2$ structure in which cation mixing has taken place. Owing to the presence of Ni or Mn ions in the Li-layer both the fringes are equally bright. Ordered and disordered rhombohedral layered $LiNiO_2$ phase is present in the thin film with diffuse coherent interface. FFTs from three different regions of interest in figure 5.10 as marked with orange, pink and blue windows are given as FFT1, FFT2 and FFT3. The projected structure of the rhombohedral layered $LiNiO_2$ when viewed along [210] zone axis is also given. The simulated diffraction pattern of the same structure along [210] zone axis is also given by the side of the FFT1. All the FFTs match quite well with the [210] zone axis pattern of the rhombohedral layered $LiNiO_2$ phase. This proves that the rhombohedral layered phase is present in the film. Additionally, it can be observed that the 003 spot from the FFT1, which comes from the orange window is very strong. This necessarily indicates that the rhombohedral layered structure is ordered in this region with completely unmixed Li-ion and (Ni/Mn)-ion layers. In the FFT2, which comes from the pink window, the 003 reciprocal lattice spot is considerably weak. This necessarily means disordering in the cation layers. Similarly, in the FFT3, which comes from the blue window, the 003 reciprocal lattice spots are even weaker. This also represents disordering in the layered phase. However, the intensity of the 003 spots in FFT2 and in FFT3 are different, which might be related to the extent of disordering in the layered structure. Similar order-disorder transformation was reported earlier [305]. However, such clear disposition of the coherent and diffused order-disorder interfaces seems to be lacking. Disordering can also be termed as the anti-site occupancy of the Li-ion and (Ni/Mn)-ions in the layered structure.

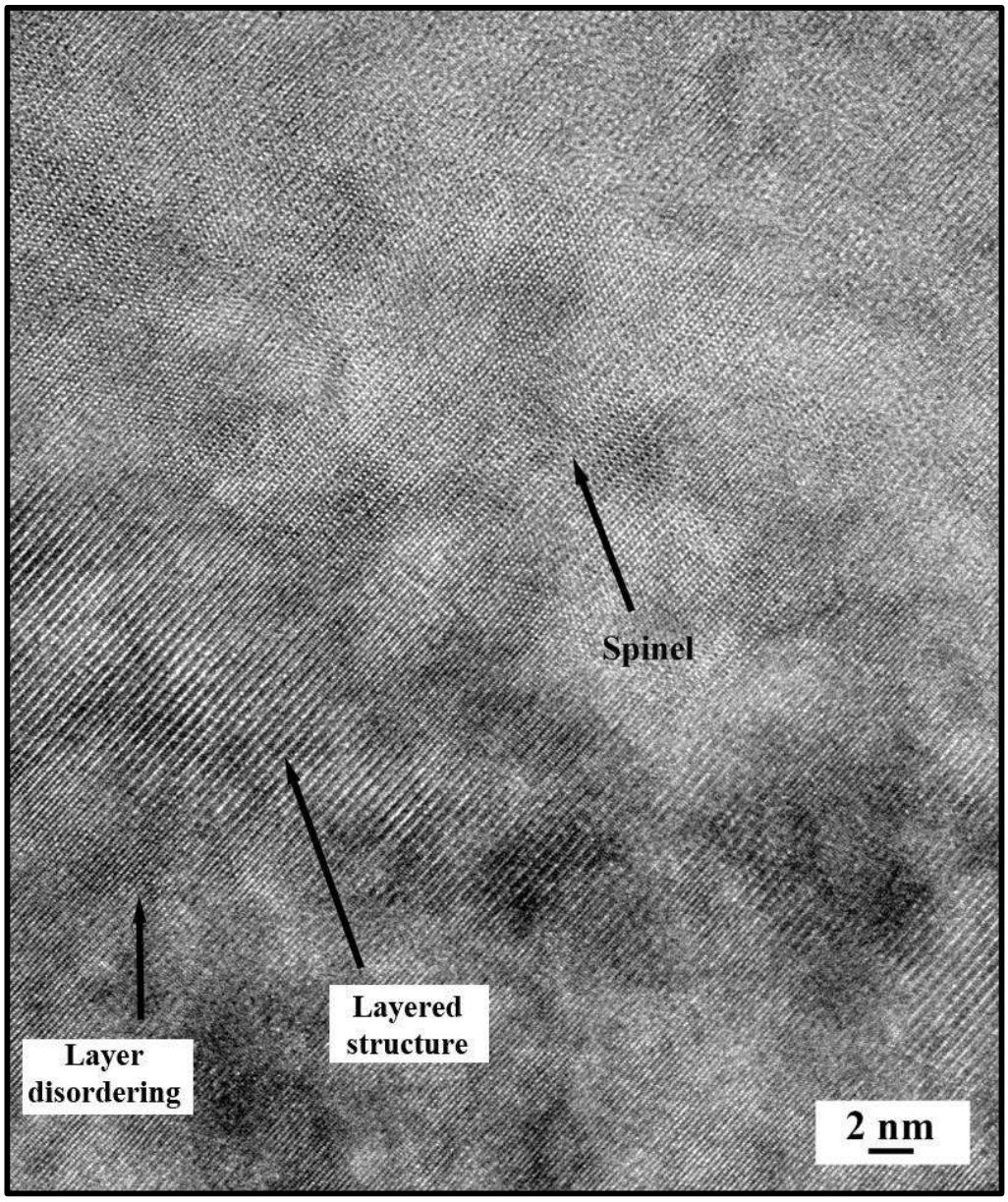

Figure 5.12: *Negative aberration-corrected high resolution phase contrast image of Li(Ni, Mn)$_x$O$_y$ thin film in which cubic Li(Ni, Mn)$_2$O$_4$ spinel, ordered rhombohedral layered Li(Ni, Mn)O$_2$ regions, disordered rhombohedral layered Li(Ni, Mn)O$_2$ regions and the coherent interface between them are observed. Representative regions are marked as 'Layer structure', 'Layer disordering' and 'Spinel'. Experimental correction parameters are C_s= (-0.00683) mm, A1=0.7246 nm, A2=46.68 nm, B2=13.8 nm, A3=295.3 nm, S3=90.35 nm.*

Negative-aberration corrected high resolution phase contrast image from another region of the film is given in figure 5.11. In this figure also, parallel fringes with 0.240 nm spacing is observed. Both the fringes are equally bright. However, for a given fringe, one notes that the spacing between two consecutive atoms changes. In one place the spacing is ~0.140 nm in other place it is ~0.290 nm. It has been mentioned earlier that in the spinel phase, in the chemically mixed layer, the spacing between two consecutive transition metal cations is doubled. The image represents a region where disordered rhombohedral layered $LiNiO_2$ and cubic $LiMn_2O_4$ phases are present. The Ni-ion and the Mn-ion could always replace each other. Moreover, it is observed that the interface between the rhombohedral layered $LiNiO_2$ phase and the cubic $LiMn_2O_4$ spinel phase is absolutely coherent. The structure changes from one to another over a couple of atom length giving rise to a diffuse coherent interface. Additional proof of the concept can be obtained from the FFTs from the orange and the blue windows as marked in the image in figure 5.11. The FFTs are given as FFT1 and FFT2 (Figure 5.11) along with the overlaid simulated patterns by their side. When the computed diffraction pattern from the [112] zone axis of the cubic $LiMn_2O_4$ spinel phase is overlaid on the FFT1 as obtained from the orange window, it matches well.

Similarly, when the simulated diffraction pattern from the [210] zone axis of the rhombohedral layered $LiNiO_2$ phase is overlaid on the FFT2 as obtained from the blue window in the image, it also matches. This proves that cubic spinel and the rhombohedral layered phases co-exist in the film. The consequence of this will be discussed in the discussion section. A relatively low-magnification negative-aberration corrected phase contrast image of the thin film is given in figure 5.12. It is observed from the image that ordered and disordered region of rhombohedral $LiNiO_2$ phase along with the spinel phase

are present in the film. The structural domains are not having any particular shape and their size varies from ~2 nm to several nanometers. However, in all the cases the interface is coherent and a typical orientation relationship is maintained between the phases.

5.4 Discussion

Core-shell or compositionally graded cathodes based on oxides have emerged as a potential cathode architecture in order to enhance life time, thermal stability, performance, and structural integrity [279,286,292]. However, structure, interfaces and microstructural constituents that may directly affect the battery performance is far from completely understood [194,287,289]. It is demonstrated in the present study that the unambiguous determination of phases, their state of ordering and interfaces is not an easy task. It has been realized that these parameters directly affect the electro-chemical activity [122,302,306]. The insight gained from the present work tries to delineate some of the issues, which are discussed in the following sub-sections.

5.4.1 Microstructure, chemistry, phases and interfaces

The thin film was deposited by pulsed laser deposition from $LiNiO_2$ and $LiMnO_x$ pellets. PLD is one of the best techniques to achieve target composition [191,220,303]. The time of deposition was altered in such a manner that it should form either a compositionally graded cathode or a core-shell cathode. Such cathodes are preferred for high capacity and structural stability of lithium batteries [279]. The analysis of cross-sectional diffraction contrast image and the diffraction pattern of the thin film confirmed the presence of phases like $LiNiMnO_4$ spinel and rhombohedral layered $LiNiO_2$ in the thin film. Observations akin to this have also been made earlier [189,307]. These phases are oriented with respect to each other in such a way that epitaxy is maintained all across the thin film. The ambiguities regarding their presence in the thin film have been confirmed with the help of tilting

experiment. Existence of these phases along with the epitaxial coherency resulted in the bigger grain size as confirmed through the diffraction pattern. This has assured that the variation in contrast all across the thin film is not arising due to the presence of grain boundaries. The contrast variation is the manifestation of strain or local composition fluctuations during the deposition of thin film [287,308]. The bigger size grains oriented in a coherent manner is considered good in terms of the structural integrity of the film [102,197]. Less grain boundary volume fraction improves the transport properties of the film [108,197,302]. Detailed compositional analysis of the film indicates that the film is nickel rich near the substrate and away from the substrate nickel and manganese are almost homogeneously distributed. Presence of lithium could be confirmed from EELS analysis. Development of core-shell structure indicates that the deposition rate of Mn is lower than that of Ni. When deposition is carried out from $LiMnO_x$ pellet for a short duration of time, almost no manganese is incorporated into the film whereas presence of nickel is always observed in the film. No significant composition fluctuation has been observed all across the film except the Ni-rich layer. The distribution of a few dark contrast features within the film surface may be attributed to the deficiency of higher atomic number species such as Ni in this case. The reason behind these local composition fluctuations is the migration of transition elements during deposition itself [171,197,309]. It is reported in literature that Ni-ion has low energy barrier for migration in Li-layer compared to the Li-ion migration within the Li-layer [302,310]. Therefore, the tendency of Ni to migrate is more compared to other transition metals. This has been reflected in the HAADF image. In the literature, researchers have shown the increased tendency of Ni segregation near the surface regions and within the grain boundaries with the help of STEM-EDS mapping and 3D-XEDS tomography [103,302]. The EELS based study of the LNMO and LMO based cathode

material have confirmed the existence of both Ni^{2+} and Ni^{3+} states in their disordered form [171]. However, the presence of Ni^{2+} ion has been proved to be detrimental to the battery performance because Ni^{2+} ion blocks the Li-ion diffusion path [292].

The film has ordered and disordered form of rhombohedral layered $Li(Ni,Mn)O_2$ phase along with the cubic $Li(Ni, Mn)_2O_4$ spinel phase. The rhombohedral phase, which is a structural derivative of rock-salt and the spinel phase, develops a particular orientation relationship with the 111 single-crystal Nb-doped $SrTiO_3$ substrate. At the same time there is an orientation relationship between the spinel phase and the rock-salt phase. The orientation relationship has been mentioned in section 5.3.1. The presence of both spinel and layered distorted rock-salt phase is considered good in providing high discharge voltage as it shows flat discharge plateau [293]. Moreover, the order-disorder structural transition in these phases has mostly been seen while moving from bulk towards the surface [306]. This is due to the mixing of transition metal cations mostly happening near the surface.

The film-substrate interface is quite sharp with no reaction product being observed at the interface. However, presence of residual strain could be ascertained at the interface. Interfaces play an important role in the overall performance of the batteries, whether it is electrolyte/cathode interface or cathode/collector interface or any other interfaces [311,312]. Interfaces govern the crystallinity and structural integrity amongst the phases which generally form in the cathode material [313,314]. Coherent interface gives good crystallinity along with improved structural integrity whereas semi- and incoherent interfaces renders poor structural integrity [102,301]. Sharpness at the interface decreases with the decrease in coherency among the homophase and heterophase interfaces [98].

The strain at the interfaces is proportional to the lattice mismatch and orientation difference. Going away from the interface reduces the effect of strain in the LNMO thin films deposited onto the substrate. These structural transformations could have been the manifestation of relaxation of strain in order to attain higher structural symmetry. These types of structural transformations have been observed in the LNMO thin films deposited on Al_2O_3 substrate [102,301]. In literature, researchers have also shown the existence of interfaces like antiphase inversion boundaries in the LNMO thin films [315]. Such antiphase inversion boundaries exist at their higher energy state compared to their stable energy state and therefore offer hindrance to the lithium intercalation process. Generally in Ni based compositions, researchers have found diffuse interfaces in the same particle with multiple domains when viewed from different projections [316]. High-resolution electron microscopy along with image simulation indicates that close to the interface the phase is mostly disordered rock-salt with almost no manganese present in that phase. However, away from the interface with the introduction of manganese into the film, formation of spinel phase along with ordered and disordered form of rock-salt is observed. The structural ordering, depending on which the cations occupy different positions in the sublattice, is the key determining factor behind structure formation. During the process of structural ordering, ordered LNMO tries to transform into the disordered LNMO and rock-salt type phases. Ordered LNMO structure is considered good for maintaining high initial capacity whereas ordered spinel decomposing into the rock-salt structure is not considered good as it deteriorates high voltage capacity [306,308]. However, ordered LNMO decomposing into disordered LNMO is considered advantageous in terms of high rate capacity. The transformation of layered $LiNiO_2$ into rock-salt type phase is considered beneficial as it provides high capacity. It can be concluded from the present study and earlier literature

that manganese tends to stabilize the spinel phase [306]. The interface between spinel and the rock-salt structure is absolutely coherent and structurally diffuse.

5.4.2 Atomic origin of electro-chemical activity

It has been observed in the present study that both the phases develop orientation relationship with the substrate. The electro-chemical activity of the film is highly sensitive to the structural parameters e.g. phase(s) evolution and interface structure [295,298,316]. From structural point of view, the electro-chemical activity of the film can be defined as the ease with which the lithium ions could be pulled out or pushed into the lattice [287]. The ordered rhombohedrally distorted Li(Ni, Mn)O_2 phase can be seen as a layered stacking of oxygen octahedra in which Ni or Mn ions are caged and in between two octahedral blocks, Li-ions are arranged (Figure 5.13a). In case of spinel phase even though the oxygen octahedra exist, such distinct layering is not observed (Figure 5.13b). The ordered rhombohedrally distorted Li(Ni, Mn)O_2 phase being layered in terms of cation arrangement, Li-ions have easier diffusion path while going in or out of the lattice under potential bias during lithiation and delithiation [302]. However, disordering in the lattice would introduce hindrances in the diffusional mobility of the Li-ions, resulting in a poisoning in the electro-chemical activity. Poisoning of electro-chemical activity in disordered rock-salt structure has been reported earlier literature [188,194,317]. In case of Li(Ni, Mn)$_2O_4$ spinel, individual cation layers do not exist and the Li-ions always have to follow a zig-zag diffusional path while charging and discharging [318]. As a result, kinetic barrier to electro-chemical activity in case of spinel is more than that of rock-salt structure. Moreover, in case of thin film cathodes, the orientation of the thin film with respect to the collector is also supposed to play an important role in determining the electrochemical activity [301,319]. Ideally, in case of rock-salt phase being present in the film, the Li-ion

layers should be perpendicular to the electron collector [102]. This orientation relationship should provide easiest diffusional path for the Li-ions under potential biasing. In the present study, it has been observed that Li-ion layers are parallel to the electron collector. This will provide further kinetic hindrance to the diffusion of Li-ions reducing the electro-chemical activity of the film [302]. The electrochemical activity also depends on the morphology of the particles in the thin film cathodes [297].

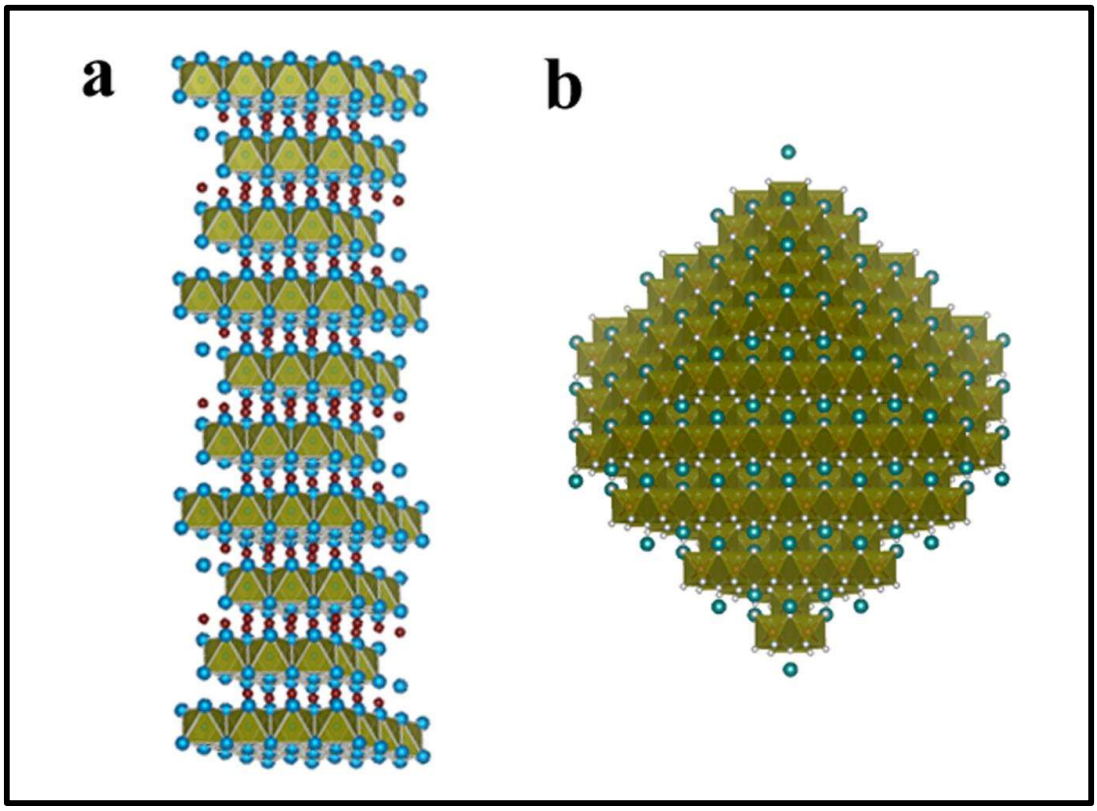

Figure 5.13: *Polyhedral representation of* ***(a)*** *rhombohedral layered $LiNiO_2$ (LNO) and (b) cubic $LiMn_2O_4$ spinel (LMO) structures. In ordered rhombohedral layered $LiNiO_2$ (LNO) layers of Li^+ ions are present between two octahedral layers of oxygen and Ni ions.*

Morphology can be controlled during the synthesis of the cathode material itself [298]. Generally, at lower temperature, it is expected to have spherical shape of the particles in the cathode materials [320]. Higher temperature synthesis of the cathode materials results

in the octahedron and truncated octahedron type of shapes [298]. The stability of truncated octahedron type of particles is more as compared to the other shapes. Moreover, truncated octahedron shaped particles show excellent electrochemical activity than cathode materials having other shaped particles. Depending on the type of shape of the particles, the ratio of surface area of 111, 100 and 110 type of facets also changes, which plays an important role in altering the electro-chemical activity of the cathode material [300]. The less strained particles have the tendency to evolve in a stable manner, which enhances the faceting behavior of the particles [320]. Earlier literature, researchers have shown that the surface energy (γ) with respect to particular facet falls in the sequence $\gamma_{111} < \gamma_{100} < \gamma_{110}$ [298,321]. In this connection, the overall bulk morphology in the thin film cathodes with respect to electrolyte and collector also effects the electrochemical activity. The bell shape morphology is considered good for the thin film cathodes because this morphology helps the electrolyte to react with the cathode material and deposit a thin layer of solid electrolyte on it by creating solid electrolyte interface (SEI) [300,322]. However, the dendritic morphology of the cathode material does not provide proper surface area to the electrolyte to react uniformly and results in the bulky deposit of SEI layer hanging to the cathode surface. Therefore, during the charging/discharging activity, this hanging SEI layer with dendritic morphology usually gets detached from the cathode and falls into the electrolyte deteriorating the electrochemical performance of the battery [299]. In the present case, the morphology in the cathode is not dendritic. However, it is not predominantly bell shaped also. It is almost single crystalline with coherent interfaces between the spinel and rock-salt phases. Suitable orientation and ordering should promote good ionic mobility and the SEI layer should form only on the surface of the film.

As stated earlier, the epitaxy in the thin film cathodes also affects the electrochemical activity in the battery [107,301]. The 111 orientation of the thin film cathode with respect to 111 orientation of the collector is considered excellent. It is reported in earlier literature that the barrier to Li-ion transport is less with this epitaxy [300]. Another importance of 111 epitaxial relationships is that the SEI layer formation on 111 planes further passivate the transition metal dissolution, whereas 110 plane does not restrict the dissolution of metal because the SEI layer on 110 plane is not stable and it breaks down pretty early leading to the dissolution of transition metals [103,300]. The epitaxy with {100} planes also shows good electrochemical activity. However, it is different from the {111} planes. The superior electrochemical activity along 111 directions is mostly attributed to the close packing. In a nutshell, it could be concluded that unfavorable orientation relationship of the film with the substrate, disordering in the rock-salt phase and the presence of cubic spinel phase are the key contributing factors, which should reduce the electro-chemical activity of such films [308,323,324].

5.4.3 Defects origin and mechanism

The presence of defects in the cathode materials has a significant influence on the performance of the batteries [195,304,325]. Generally, the higher concentration of defects in the cathodes provide lot of hindrance to the intercalation/ deintercalation of Li-ion, induces order-disorder structural transformation, enhances segregation of transition metal ions etc. [102,314,315,322,325]. All these activities occurring inside the cathode material reduces the voltage capacity, rate capacity, cyclability, lifetime etc., of the batteries. Therefore, determining the origin of defects as well as understanding the underlying mechanism behind it to alleviate its presence are the key steps to improve the battery performance. Limited information is available on the evolution of defects in the thin film

cathodes and their effects on the battery performance [315,325]. One way to alleviate the detrimental effects of defects is to coat the cathode surface [326]. These coatings are done either by mixing the surfactants like Poly- ethylene Glycol (PEG), Trietanolamine (TEA) etc., during the synthesis of the cathode material itself or by depositing the thin layer of $LiPO_4$, SiO_2 etc., onto the thin film cathode. It has been also reported that oxygen deficiency during high temperature synthesis process promotes the vacancy formation which in turn leads to a change in the oxidation state of the transition metals [193,287,327,328]. The presence of moisture enhances the segregation tendency of Ni^{2+} towards oxygen since the bonding affinity between them is quite high [280]. However, increased surface to volume ratio also increases the surface segregation due to the enhanced surface energy mediated diffusion. The annealed collector material also shows some uniformly spaced kinks at the surface, therefore during deposition of thin film cathodes this results in the formation of antiphase inversion domains boundaries[315]. During the synthesis of cathode material if various domains with lost point group symmetry are formed within the same particle than it would result in the rotational boundaries when observed from the same zone [107]. In our case, the PLD deposited core-shell cathode thin film has less concentration of defects as could be seen all across the thin film (cf. Figure 5.2a). There is no signature of grain boundaries, dislocations etc., as could be observed in the diffraction contrast, HAADF and HRTEM image. The possibility of grain boundaries has been ruled out due to the higher degree of epitaxy and the thin film integrity. The observation is limited in the TEM/STEM observational length scales. Further investigation may be done by SEM and EBSD, which might be able to resolve grain boundaries and interfaces at much coarser length scale. However, residual strain could be ascertained by the bending of lattice fringes at the film/substrate interface in figure 5.4a. While moving gradually towards the surface from

the interface, the cross lattice fringes with high contrast and resolved atomic columns could be observed in HRTEM images (cf. Figure 5.5(a-c)). This may be expected due to the intermixing of transition metal ions. On the basis of above discussion, it can be concluded that there exists a plethora of possibilities of defect formation depending on the chemistry, synthesis method, synthesis temperature etc. However, the solutions to the mass elimination of defects could be addition of surfactants to the cathode material, passivation coatings and PLD technique. The underlying mechanism suggested above is satisfying and proved to be significant in reducing the large defects concentration.

5.5 Conclusions

1. PLD deposition of $LiNiO_2$ and $LiMnO_x$ onto 111 single-crystal Nb:STO substrate leads to the formation of a core-shell oxide thin film which is rich in Ni at the interface. This is due to the difference in deposition rate of Ni and Mn onto the substrate at the deposition temperature.
2. Rhombohedrally distorted layered $Li(Ni, Mn)O_2$ and cubic $Li(Ni, Mn)_2O_4$ phases are observed in the film. There is an orientation relationship between the substrate and the film. The orientation relationship between the STO substrate and the spinel phase is $[112]_{STO}\|[112]_{Spinel}$ and $(\bar{1}\bar{1}1)_{STO}\|(\bar{1}\bar{1}1)_{Spinel}$ and that with $Li(Ni,Mn)O_2$ is $[112]_{STO}\|[210]_{LiNiO2}$ and $(\bar{1}\bar{1}1)_{STO}\|(00\bar{3})_{LiNiO2}$. The orientation relationship between the spinel phase and the $Li(Ni,Mn)O_2$ phase is $[112]_{Spinel}\|[210]_{LiNiO2}$ and $(\bar{1}\bar{1}1)_{Spinel}\|(00\bar{3})_{LiNiO2}$. Nominal amount of strain is present at the film substrate interface. However, extensive defect formation is not observed.
3. Cubic $Li(Ni, Mn)_2O_4$ spinel and rhombohedrally distorted layered $Li(Ni, Mn)O_2$ phases are quite similar in the reciprocal space. However, it is possible to

distinguish the phases by high-resolution imaging and quantification of the spacing between two octahedrally located cations. In case of spinel, the spacing between two octahedrally located cations is just double than the rhombohedrally distorted layered $Li(Ni,Mn)O_2$ structure.

4. In the $Li(Ni, Mn)O_2$ phase ordered and disordered domains are present. The interface between the order-disorder domains and that between $Li(Ni, Mn)O_2$ and spinel are absolutely coherent and diffuse. The electro-chemical activity of such film is not likely to be optimum because of the wrong orientation relationship, presence of spinel phase and also due to the presence of cation disordered domains in the $Li(Ni, Mn)O_2$ phase.